Commun. Comput. Phys.
doi: 10.4208/cicp.OA-2020-0096

Vol. **29**, No. 4, pp. 1030-1058
April 2021

High-Order Runge-Kutta Discontinuous Galerkin Methods with a New Type of Multi-Resolution WENO Limiters on Tetrahedral Meshes

Jun Zhu[1], Chi-Wang Shu[2] and Jianxian Qiu[3,*]

[1] *College of Science, Nanjing University of Aeronautics and Astronautics, Nanjing, Jiangsu 210016, P.R. China.*
[2] *Division of Applied Mathematics, Brown University, Providence, RI 02912, USA.*
[3] *School of Mathematical Sciences and Fujian Provincial Key Laboratory of Mathematical Modeling and High-Performance Scientific Computing, Xiamen University, Xiamen, Fujian 361005, P.R. China.*

Received 25 May 2020; Accepted (in revised version) 13 November 2020

Abstract. In this paper, the second-order and third-order Runge-Kutta discontinuous Galerkin (RKDG) methods with multi-resolution weighted essentially non-oscillatory (WENO) limiters are proposed on tetrahedral meshes. The multi-resolution WENO limiter is an extension of a finite volume multi-resolution WENO scheme developed in [81], which serves as a limiter for RKDG methods on tetrahedral meshes. This new WENO limiter uses information of the DG solution essentially only within the troubled cell itself which is identified by a new modified version of the original KXRCF indicator [42], to build a sequence of hierarchical L^2 projection polynomials from zeroth degree to the second or third degree of the DG solution. The second-order and third-order RKDG methods with the associated multi-resolution WENO limiters are developed as examples for general high-order RKDG methods, which could maintain the original order of accuracy in smooth regions and keep essentially non-oscillatory property near strong discontinuities by gradually degrading from the optimal order to the first order. The linear weights inside the procedure of the new multi-resolution WENO limiters can be set as any positive numbers on the condition that they sum to one. A series of polynomials of different degrees within the troubled cell itself are applied in a WENO fashion to modify the DG solutions in the troubled cell on tetrahedral meshes. These new WENO limiters are very simple to construct, and can be easily implemented to arbitrary high-order accuracy on tetrahedral meshes. Such spatial reconstruction methodology improves the robustness in the simulation on the same compact spatial stencil of the original DG methods on tetrahedral meshes. Extensive one-dimensional (run as three-dimensional problems on tetrahedral meshes) and three-dimensional tests are performed to demonstrate the good performance of the RKDG methods with new multi-resolution WENO limiters.

*Corresponding author. *Email addresses:* zhujun@nuaa.edu.cn (J. Zhu), chi-wang_shu@brown.edu (C.-W. Shu), jxqiu@xmu.edu.cn (J. Qiu)

AMS subject classifications: 65M60, 65M99, 35L65

Key words: Runge-Kutta discontinuous Galerkin method, multi-resolution WENO limiter, tetrahedral mesh.

1 Introduction

In this paper, three-dimensional hyperbolic conservation laws

$$\begin{cases} u_t+f(u)_x+g(u)_y+r(u)_z=0, \\ u(x,y,z,0)=u_0(x,y,z), \end{cases} \tag{1.1}$$

are considered and the Runge-Kutta discontinuous Galerkin (RKDG) methods [13–15, 17] with new multi-resolution WENO limiters are applied to solve (1.1) on tetrahedral meshes. The DG methods are applied to discretize the spatial variables and explicit, nonlinearly stable high-order Runge-Kutta methods [12, 18, 38, 48, 64, 66] are adopted to discretize the temporal variable. The main objective of this paper is to design new second-order and third-order spatial limiting procedures to obtain uniform accuracy in smooth regions and obtain sharp and non-oscillatory shock transitions in non-smooth regions for high-order RKDG methods. This new methodology can be applied to design high-order WENO limiting procedures for any high-order RKDG methods on tetrahedral meshes, however we will use only second-order and third-order cases in this paper as examples.

Let us first review the history of the development of discontinuous Galerkin (DG) methods. In 1973, Reed and Hill [62] designed the first DG method in the framework of neutron transport. Due to its desirable properties, many developed DG methods were also used in atmospheric science with an extensive list of references [2, 29–31, 55–57]. The reconstruction operator [21,22] was applied at the beginning of each time step in the computation to increase the formal order of accuracy of high-order DG methods. Lagrangian DG methods were proposed for the first time in [49, 53, 68–70]. A Taylor basis was used in [40] for the development of a discontinuous Galerkin spectral finite element method. More recently, a new novel weighted Runge-Kutta discontinuous Galerkin method [37] is proposed for solving three-dimensional acoustic and elastic wave and reconstructed discontinuous Galerkin (rDG) method [51, 52] is presented for solving diffusion equations. Other new contributions to design high-order DG methods can also be found in [10, 11, 45]. But if problems are not smooth enough, the associated numerical solution would have spurious oscillations near strong shocks or contact discontinuities and could result in the appearances of nonlinear instability in non-smooth regions. One possible methodology to suppress such spurious oscillations is to apply nonlinear limiters to the RKDG methods. A major development of the DG method with a classical *minmod* type total variation bounded (TVB) limiter was carried out by Cockburn et al. in a series of papers [13–17] to solve nonlinear time dependent hyperbolic conservation laws

together with the application of explicit, nonlinearly stable high-order Runge-Kutta time discretization [66]. Such methods are termed as RKDG methods. One type of limiters is based on slope modification, such as classical *minmod* type limiters [13–15, 17], the moment based limiter [3], and an improved moment limiter [7], and so on. Such limiters belong to the slope type limiters and they could suppress spurious oscillations at the price of possibly degrading optimal numerical accuracy at smooth extrema. Another type of limiters is based on the essentially non-oscillatory (ENO) and weighted ENO (WENO) methodologies [27, 39, 41, 50, 63], which can achieve high-order accuracy in smooth regions and keep essentially non-oscillatory property near strong discontinuities. These WENO limiters are basically designed in a finite volume WENO fashion, but they need a wider spatial stencil for obtaining high-order schemes. Other WENO limiters have also been applied for DG methods [1,58,59,61,73]. The WENO limiters [54,59,60,77], adaptive-order WENO limiters [5], central WENO (CWENO) limiters [6], and Hermite WENO limiters [58,61,74] belong to the second type of limiters. Since CWENO schemes [19,20,23,46] are computationally less expensive than the WENO reconstruction algorithms [24–26], they can serve as a posteriori subcell limiters for DG schemes [56]. However, it is very difficult to implement RKDG methods with the applications of unstructured WENO limiters, CWENO limiters, or Hermite WENO limiters for solving compressible three-dimensional problems on tetrahedral meshes.

Recently, a new type of finite difference or finite volume multi-resolution WENO schemes is designed in [79–81] for solving hyperbolic conservation laws. They only apply the information defined on a hierarchy of nested central spatial stencils to perform spatial discretization procedures and do not introduce any equivalent multi-resolution representation [32–36]. These new multi-resolution WENO schemes adopt the same largest stencil and apply a smaller number of stencils in designing high-order spatial approximation procedures than that of the classical WENO schemes in [39, 72] on triangular meshes or tetrahedral meshes, could obtain the optimal order of accuracy in smooth regions, and could gradually degrade from the optimal order to first-order accuracy near strong discontinuities. The linear weights of them in the spatial reconstruction procedures can be any positive numbers on the condition that they sum to one. In this paper, which is a continuation of [76,78], we extend high-order RKDG methods with new multi-resolution WENO limiters from structured meshes and triangular meshes to tetrahedral meshes. Two major advantages of these multi-resolution WENO limiters are the compactness of their spatial stencil, which essentially only contain the tetrahedral troubled cell itself with information from the four neighboring tetrahedral cells used only to determine the smoothness indicator of the zeroth degree polynomial in the hierarchy, and the simplicity in the implementation. In order to keep the advantages of the compact stencil and simplicity of linear weights, we make a small modification of the procedure in [79–81], by using orthogonal basis and L^2 projection to define the sequence of hierarchical polynomials of different degrees in the tetrahedral troubled cell. This modification facilitates the achievement of strict conservation and the maintenance of as much information of the original polynomial in the tetrahedral troubled cell as possible through the

mechanism of a gradual degradation to lower degree polynomials in an L^2 projection fashion with the spatial WENO procedure on tetrahedral meshes.

This paper is organized as follows. In Section 2, the RKDG methods for solving (1.1) are briefly reviewed on tetrahedral meshes. In Section 3, the details of the new multi-resolution WENO procedure for three-dimensional scalar and hyperbolic conservation laws are presented on tetrahedral meshes. Numerical examples are provided in Section 4 to verify the compactness, accuracy, and stability of this new approach. Concluding remarks are finally given in Section 5.

2 Review of the RKDG method on tetrahedral meshes

Given the tetrahedral cell Δ_j, $\mathbb{P}^k(\Delta_j)$ denotes the set of polynomials of degree at most k defined on Δ_j. Here k could actually change from cell to cell (p-adaptivity), but for simplicity we assume it is a constant in this paper. In the DG method, the solution as well as the test function space is given by $W_h^k=\{v(x,y,z):v(x,y,z)|_{\Delta_j}\in\mathbb{P}^k(\Delta_j)\}$. We emphasize that the procedure described below does not depend on the specific basis chosen for the polynomials. We adopt a local orthogonal basis over the target tetrahedral cell, such as Δ_0: $\{v_l^{(0)}(x,y,z),\ l=0,\cdots,K_k;\ K_k=\frac{(k+1)(k+2)(k+3)}{6}-1\}$:

$$
\begin{aligned}
v_0^{(0)}(x,y,z)&=1,\\
v_1^{(0)}(x,y,z)&=\frac{(x-x_0)}{|\Delta_0|^{1/3}},\\
v_2^{(0)}(x,y,z)&=a_{21}\frac{(x-x_0)}{|\Delta_0|^{1/3}}+\frac{(y-y_0)}{|\Delta_0|^{1/3}}+a_{22},\\
v_3^{(0)}(x,y,z)&=a_{31}\frac{(x-x_0)}{|\Delta_0|^{1/3}}+a_{32}\frac{(y-y_0)}{|\Delta_0|^{1/3}}+\frac{(z-z_0)}{|\Delta_0|^{1/3}}+a_{33},\\
v_4^{(0)}(x,y,z)&=a_{41}\frac{(x-x_0)}{|\Delta_0|^{1/3}}+a_{42}\frac{(y-y_0)}{|\Delta_0|^{1/3}}+a_{43}\frac{(z-z_0)}{|\Delta_0|^{1/3}}+\frac{(x-x_0)^2}{|\Delta_0|^{2/3}}+a_{44},\\
v_5^{(0)}(x,y,z)&=a_{51}\frac{(x-x_0)}{|\Delta_0|^{1/3}}+a_{52}\frac{(y-y_0)}{|\Delta_0|^{1/3}}+a_{53}\frac{(z-z_0)}{|\Delta_0|^{1/3}}+a_{54}\frac{(x-x_0)^2}{|\Delta_0|^{2/3}}\\
&\quad+\frac{(x-x_0)(y-y_0)}{|\Delta_0|^{2/3}}+a_{55},\\
v_6^{(0)}(x,y,z)&=a_{61}\frac{(x-x_0)}{|\Delta_0|^{1/3}}+a_{62}\frac{(y-y_0)}{|\Delta_0|^{1/3}}+a_{63}\frac{(z-z_0)}{|\Delta_0|^{1/3}}+a_{64}\frac{(x-x_0)^2}{|\Delta_0|^{2/3}}\\
&\quad+a_{65}\frac{(x-x_0)(y-y_0)}{|\Delta_0|^{2/3}}+\frac{(x-x_0)(z-z_0)}{|\Delta_0|^{2/3}}+a_{66},
\end{aligned}
$$

$$
\begin{aligned}
v_7^{(0)}(x,y,z) =& a_{71}\frac{(x-x_0)}{|\Delta_0|^{1/3}}+a_{72}\frac{(y-y_0)}{|\Delta_0|^{1/3}}+a_{73}\frac{(z-z_0)}{|\Delta_0|^{1/3}}+a_{74}\frac{(x-x_0)^2}{|\Delta_0|^{2/3}}\\
&+a_{75}\frac{(x-x_0)(y-y_0)}{|\Delta_0|^{2/3}}+a_{76}\frac{(x-x_0)(z-z_0)}{|\Delta_0|^{2/3}}+\frac{(y-y_0)^2}{|\Delta_0|^{2/3}}+a_{77},\\
v_8^{(0)}(x,y,z) =& a_{81}\frac{(x-x_0)}{|\Delta_0|^{1/3}}+a_{82}\frac{(y-y_0)}{|\Delta_0|^{1/3}}+a_{83}\frac{(z-z_0)}{|\Delta_0|^{1/3}}+a_{84}\frac{(x-x_0)^2}{|\Delta_0|^{2/3}}\\
&+a_{85}\frac{(x-x_0)(y-y_0)}{|\Delta_0|^{2/3}}+a_{86}\frac{(x-x_0)(z-z_0)}{|\Delta_0|^{2/3}}+a_{87}\frac{(y-y_0)^2}{|\Delta_0|^{2/3}}\\
&+\frac{(y-y_0)(z-z_0)}{|\Delta_0|^{2/3}}+a_{88},\\
v_9^{(0)}(x,y,z) =& a_{91}\frac{(x-x_0)}{|\Delta_0|^{1/3}}+a_{92}\frac{(y-y_0)}{|\Delta_0|^{1/3}}+a_{93}\frac{(z-z_0)}{|\Delta_0|^{1/3}}+a_{94}\frac{(x-x_0)^2}{|\Delta_0|^{2/3}}\\
&+a_{95}\frac{(x-x_0)(y-y_0)}{|\Delta_0|^{2/3}}+a_{96}\frac{(x-x_0)(z-z_0)}{|\Delta_0|^{2/3}}+a_{97}\frac{(y-y_0)^2}{|\Delta_0|^{2/3}}\\
&+a_{98}\frac{(y-y_0)(z-z_0)}{|\Delta_0|^{2/3}}+\frac{(z-z_0)^2}{|\Delta_0|^{2/3}}+a_{99},\\
&\cdots
\end{aligned}
$$

where (x_0,y_0,z_0) and $|\Delta_0|$ are the volume barycenter and the volume of the target tetrahedral cell Δ_0, respectively. Then we would need to solve a linear system to obtain the values of a_* by the orthogonality property:

$$\int_{\Delta_0} v_i^{(0)}(x,y,z)v_j^{(0)}(x,y,z)dxdydz = w_i\delta_{ij}, \tag{2.1}$$

with $w_i = \int_{\Delta_0}\left(v_i^{(0)}(x,y,z)\right)^2 dxdydz$.

The numerical solution $u_h(x,y,z,t)$ in the space W_h^k can be written as:

$$u_h(x,y,z,t) = \sum_{l=0}^{K_k} u_0^{(l)}(t)v_l^{(0)}(x,y,z), \quad \text{for } (x,y,z)\in\Delta_0,$$

and the degrees of freedom $u_0^{(l)}(t)$ are the moments defined by:

$$u_0^{(l)}(t) = \frac{1}{w_l}\int_{\Delta_0} u_h(x,y,z,t)v_l^{(0)}(x,y,z)dxdydz, \quad l=0,\cdots,K_k.$$

In order to determine the approximate solution, we evolve the degrees of freedom $u_0^{(l)}(t)$:

$$\begin{aligned}\frac{d}{dt}u_0^{(l)}(t)=&\frac{1}{w_l}\left(\int_{\Delta_0}\left(f(u_h(x,y,z,t))\frac{\partial}{\partial x}v_l^{(0)}(x,y,z)+g(u_h(x,y,z,t))\frac{\partial}{\partial y}v_l^{(0)}(x,y,z)\right.\right.\\&\left.+r(u_h(x,y,z,t))\frac{\partial}{\partial z}v_l^{(0)}(x,y,z)\right)dxdydz\\&\left.+\int_{\partial\Delta_0}(f(u_h(x,y,z,t)),g(u_h(x,y,z,t)),r(u_h(x,y,z,t)))\cdot n\,v_l^{(0)}(x,y,z)ds\right),\\&l=0,\cdots,K_k,\end{aligned}\tag{2.2}$$

where n is the outward unit normal of the boundary $\partial\Delta_0$.

In (2.2) the integral terms can be computed either exactly or by suitable numerical quadratures. In this paper, we use A_G points ($A_G=5$ for $k=1$ and $A_G=16$ for $k=2$) for the volume quadrature and E_G points ($E_G=6$ for $k=1,2$) for the face quadrature:

$$\begin{aligned}&\int_{\Delta_0}\left(f(u_h(x,y,z,t))\frac{\partial}{\partial x}v_l^{(0)}(x,y,z)+g(u_h(x,y,z,t))\frac{\partial}{\partial y}v_l^{(0)}(x,y,z)\right.\\&\left.+r(u_h(x,y,z,t))\frac{\partial}{\partial z}v_l^{(0)}(x,y,z)\right)dxdydz\\\approx&|\Delta_0|\sum_{\ell=1}^{A_G}\sigma_\ell\left(f(u_h(\bar{x}_\ell,\bar{y}_\ell,\bar{z}_\ell,t))\frac{\partial}{\partial x}v_l^{(0)}(\bar{x}_\ell,\bar{y}_\ell,\bar{z}_\ell)\right.\\&\left.+g(u_h(\bar{x}_\ell,\bar{y}_\ell,\bar{z}_\ell,t))\frac{\partial}{\partial y}v_l^{(0)}(\bar{x}_\ell,\bar{y}_\ell,\bar{z}_\ell)+r(u_h(\bar{x}_\ell,\bar{y}_\ell,\bar{z}_\ell,t))\frac{\partial}{\partial z}v_l^{(0)}(\bar{x}_\ell,\bar{y}_\ell,\bar{z}_\ell)\right),\end{aligned}\tag{2.3}$$

$$\begin{aligned}&\int_{\partial\Delta_0}(f(u_h(x,y,z,t)),g(u_h(x,y,z,t)),r(u_h(x,y,z,t)))\cdot n\,v_l^{(0)}(x,y,z)ds\\\approx&\sum_{ll=1}^{4}|\partial\Delta_{0_{ll}}|\sum_{\ell=1}^{E_G}\bar{\sigma}_\ell(f(u_h(\bar{x}_{ll_\ell},\bar{y}_{ll_\ell},\bar{z}_{ll_\ell},t)),g(u_h(\bar{x}_{ll_\ell},\bar{y}_{ll_\ell},\bar{z}_{ll_\ell},t)),\\&\qquad r(u_h(\bar{x}_{ll_\ell},\bar{y}_{ll_\ell},\bar{z}_{ll_\ell},t)))\cdot n_{ll}\,v_l^{(0)}(\bar{x}_{ll_\ell},\bar{y}_{ll_\ell},\bar{z}_{ll_\ell}),\end{aligned}\tag{2.4}$$

where $(\bar{x}_\ell,\bar{y}_\ell,\bar{z}_\ell)\in\Delta_0$ and $(\bar{x}_{ll_\ell},\bar{y}_{ll_\ell},\bar{z}_{ll_\ell})\in\partial\Delta_{0_{ll}}$ are the quadrature points, and σ_ℓ and $\bar{\sigma}_\ell$ are the quadrature weights. The volume integrals in (2.3) are discretized by a quadrature integration formula on every tetrahedral element (for example, $A_G=5$ for $k=1$ and Δ_0 has four vertexes (x_1,y_1,z_1), (x_2,y_2,z_2), (x_3,y_3,z_3), and (x_4,y_4,z_4), the five-point quadrature points are

$$\begin{aligned}(\bar{x}_1,\bar{y}_1,\bar{z}_1)&=(\lambda_1x_1+\lambda_2x_2+\lambda_2x_3+\lambda_2x_4,\lambda_1y_1+\lambda_2y_2+\lambda_2y_3+\lambda_2y_4,\lambda_1z_1+\lambda_2z_2+\lambda_2z_3+\lambda_2z_4),\\(\bar{x}_2,\bar{y}_2,\bar{z}_2)&=(\lambda_2x_1+\lambda_1x_2+\lambda_2x_3+\lambda_2x_4,\lambda_2y_1+\lambda_1y_2+\lambda_2y_3+\lambda_2y_4,\lambda_2z_1+\lambda_1z_2+\lambda_2z_3+\lambda_2z_4),\\(\bar{x}_3,\bar{y}_3,\bar{z}_3)&=(\lambda_2x_1+\lambda_2x_2+\lambda_1x_3+\lambda_2x_4,\lambda_2y_1+\lambda_2y_2+\lambda_1y_3+\lambda_2y_4,\lambda_2z_1+\lambda_2z_2+\lambda_1z_3+\lambda_2z_4),\\(\bar{x}_4,\bar{y}_4,\bar{z}_4)&=(\lambda_2x_1+\lambda_2x_2+\lambda_2x_3+\lambda_1x_4,\lambda_2y_1+\lambda_2y_2+\lambda_2y_3+\lambda_1y_4,\lambda_2z_1+\lambda_2z_2+\lambda_2z_3+\lambda_1z_4),\\(\bar{x}_5,\bar{y}_5,\bar{z}_5)&=(\beta_1x_1+\beta_1x_2+\beta_1x_3+\beta_1x_4,\beta_1y_1+\beta_1y_2+\beta_1y_3+\beta_1y_4,\beta_1z_1+\beta_1z_2+\beta_1z_3+\beta_1z_4),\end{aligned}$$

where $\lambda_1=\frac{1}{2}$, $\lambda_2=\frac{1}{6}$, $\beta_1=\frac{1}{4}$, and the quadrature weights are $\sigma_1=\frac{9}{20}$, $\sigma_2=\frac{9}{20}$, $\sigma_3=\frac{9}{20}$, $\sigma_4=\frac{9}{20}$, and $\sigma_5=-\frac{4}{5}$). The surface integrals in (2.4) are discretized by a quadrature integration formula on every triangular element (for example, $E_G=6$ for $k=1,2$ and a triangular element $\partial\Delta_{0_{ll}}$ has three vertexes (x_1,y_1,z_1), (x_2,y_2,z_2), and (x_3,y_3,z_3), the six-point quadrature points are

$$
\begin{aligned}
&(\bar{x}_{ll_1},\bar{y}_{ll_1},\bar{z}_{ll_1})=(\lambda_1x_1+\lambda_2x_2+\lambda_2x_3,\lambda_1y_1+\lambda_2y_2+\lambda_2y_3,\lambda_1z_1+\lambda_2z_2+\lambda_2z_3),\\
&(\bar{x}_{ll_2},\bar{y}_{ll_2},\bar{z}_{ll_2})=(\lambda_2x_1+\lambda_1x_2+\lambda_2x_3,\lambda_2y_1+\lambda_1y_2+\lambda_2y_3,\lambda_2z_1+\lambda_1z_2+\lambda_2z_3),\\
&(\bar{x}_{ll_3},\bar{y}_{ll_3},\bar{z}_{ll_3})=(\lambda_2x_1+\lambda_2x_2+\lambda_1x_3,\lambda_2y_1+\lambda_2y_2+\lambda_1y_3,\lambda_2z_1+\lambda_2z_2+\lambda_1z_3),\\
&(\bar{x}_{ll_4},\bar{y}_{ll_4},\bar{z}_{ll_4})=(\beta_1x_1+\beta_2x_2+\beta_2x_3,\beta_1y_1+\beta_2y_2+\beta_2y_3,\beta_1z_1+\beta_2z_2+\beta_2z_3),\\
&(\bar{x}_{ll_5},\bar{y}_{ll_5},\bar{z}_{ll_5})=(\beta_2x_1+\beta_1x_2+\beta_2x_3,\beta_2y_1+\beta_1y_2+\beta_2y_3,\beta_2z_1+\beta_1z_2+\beta_2z_3),\\
&(\bar{x}_{ll_6},\bar{y}_{ll_6},\bar{z}_{ll_6})=(\beta_2x_1+\beta_2x_2+\beta_1x_3,\beta_2y_1+\beta_2y_2+\beta_1y_3,\beta_2z_1+\beta_2z_2+\beta_1z_3),
\end{aligned}
$$

where

$$
\begin{aligned}
&\lambda_1=0.816847572980459, \quad \lambda_2=0.091576213509771,\\
&\beta_1=0.108103018168070, \quad \beta_2=0.445948490915965,
\end{aligned}
$$

and the quadrature weights are $\bar{\sigma}_1=\bar{\sigma}_2=\bar{\sigma}_3=0.109951743655322$ and $\bar{\sigma}_4=\bar{\sigma}_5=\bar{\sigma}_6=0.22338158967\ 8011$). Since the face integral is on boundaries where the numerical solution is discontinuous, the flux $(f(u_h(x,y,z,t)),g(u_h(x,y,z,t)),r(u_h(x,y,z,t)))\cdot n$ is replaced by a monotone numerical flux in the scalar case or by an exact or approximate Riemann solver based numerical flux for the system case. The simple Lax-Friedrichs flux is used in all of our numerical tests. The semi-discrete scheme (2.2) is discretized in time by a nonlinear stable Runge-Kutta time discretization, e.g. the third-order version [66]:

$$
\begin{cases}
u^{(1)}=u^n+\Delta tL(u^n),\\
u^{(2)}=\frac{3}{4}u^n+\frac{1}{4}u^{(1)}+\frac{1}{4}\Delta tL(u^{(1)}),\\
u^{n+1}=\frac{1}{3}u^n+\frac{2}{3}u^{(2)}+\frac{2}{3}\Delta tL(u^{(2)}).
\end{cases}
\tag{2.5}
$$

The method described above can compute solutions to (1.1), which are either smooth or have weak shocks and other discontinuities, without further modification. If the discontinuities are strong, however, the scheme will generate significant oscillations and even nonlinear instability. To avoid such difficulties, we borrow the technique of a slope limiter from the finite volume methodology and use it after each Runge-Kutta inner stage to control the numerical solution. For the purpose of explaining how to apply a nonlinear limiter for the RKDG methods as shown in [73], we adopt a forward Euler time discretization of (2.2) as an example. In this three-dimensional case, starting from a solution $u_h^n\in W_h^k$ at time level n, it is limited to obtain a new function $u_h^{n,new}$ before advancing

it to the next time level. We need to find $u_h^{n+1}\in W_h^k$ which satisfies

$$\int_{\Delta_0}\frac{u_h^{n+1}-u_h^{n,new}}{\Delta t}v\,dxdydz-\int_{\Delta_0}\left(f(u_h^{n,new})v_x+g(u_h^{n,new})v_y+r(u_h^{n,new})v_z\right)dxdydz$$
$$+\int_{\partial\Delta_0}\left(\hat{f}(u_h^{n,new}),\hat{g}(u_h^{n,new}),\hat{r}(u_h^{n,new})\right)\cdot nv\,ds=0, \tag{2.6}$$

for all test functions $v(x,y,z)\in W_h^k$. We will focus on how to obtain the three-dimensional $u_h^{n,new}|_{\Delta_0}$ and omit its sup-index n in the following, if it does not cause confusion.

3 Multi-resolution WENO limiter on tetrahedral meshes

In this section, we focus on designing a new multi-resolution WENO reconstruction procedure as a limiter for the second-order and third-order RKDG methods on tetrahedral meshes. It is an extension to tetrahedral meshes of the high-order limiting procedure that was developed in [76, 78] on structured meshes and triangular meshes. The main framework of the new multi-resolution WENO limiting procedure on tetrahedral cells is narrated in the following.

3.1 The new three-dimensional modified KXRCF shock detection technique

The main purpose of this subsection is to precisely detect the troubled cells, which may need the new multi-resolution WENO limiting procedure later. This detective procedure is important for designing limiters. If excessive tetrahedral cells are detected as troubled cells, the computational cost will increase. If too few tetrahedral cells are identified as troubled cells, spurious oscillations may appear in non-smooth regions. Since a comparison among different troubled cell indicators was given in [60], the classical KXRCF shock detection technique [42] has been widely used in detecting troubled cells, which are cells that may contain strong shocks or contact discontinuities and in which the multi-resolution WENO limiter is applied. We now propose a new three-dimensional modified version of the classical KXRCF shock detection technique [42] to detect troubled cells on tetrahedral meshes. As shown in [42], we will divide the boundary of the tetrahedral cell Δ_j into two parts: $\partial\Delta_j^-$ and $\partial\Delta_j^+$, where the flow is into and out of Δ_j, respectively. In the one-dimensional case, Fu and Shu [28] noted that the scaling of $|x_{j+\frac{1}{2}}-x_{j-\frac{1}{2}}|^{\frac{k+1}{2}}$ tends to mark a lot more troubled cells than necessary for high-order DG methods. They decreased the power of $|x_{j+\frac{1}{2}}-x_{j-\frac{1}{2}}|$ to be $\frac{\min(k,2)+1}{2}$, which seems to be strong enough to single out discontinuities [28]. Now on tetrahedral meshes, we define the tetrahedral cell Δ_0 as a troubled cell on the condition that

$$\frac{|\int_{\partial\Delta_0^-}(u_h(x,y,z,t)|_{\Delta_0}-u_h(x,y,z,t)|_{\Delta_l})ds|}{h_0^R|\partial\Delta_0^-|\cdot|||\widehat{u_h}(x,y,z,t)|_{\partial\Delta_0}|||}\geq C_k, \tag{3.1}$$

where $R=1$ for $k=1$ and $R=1.5$ for $k>1$, h_0 is the radius of the circumscribed circle in the tetrahedral cell Δ_0, and C_k is a constant, usually, we take $C_k=1$ as specified in [42]. Here Δ_l, l is chosen as 1, or 2, or 3, or 4, which denotes the neighboring tetrahedral cells of Δ_0 on the side of $\partial\Delta_0^-$. $u_h(x,y,z,t)$ is the numerical solution corresponding to the indicator variable(s) and $|||\widehat{u_h}(x,y,z,t)|_{\partial\Delta_0}|||$ is defined as the minimum value of $|u_h(x,y,z,t)|$ along $\partial\Delta_0$. By using (3.1), we do not need to adopt different types of C_k to compute multi-dimensional test problems as specified in [28] and can simply set $C_k=1$ in all numerical computations, unless specified otherwise. This new three-dimensional modified KXRCF shock detection technique is simple and robust enough to catch strong discontinuities without identifying excessive troubled cells on tetrahedral meshes.

3.2 Multi-resolution WENO reconstruction

The objective of this subsection is to reconstruct a new polynomial using the multi-resolution WENO limiting procedure to replace the solution polynomial on the troubled cell. The new polynomial should maintain the cell average and high-order accuracy of the original DG solution without introducing oscillations on tetrahedral meshes.

First, the details of the new multi-resolution WENO limiting procedure are presented for the scalar case. The basic idea is to reconstruct a new polynomial on the troubled cell Δ_0 which is a convex combination of polynomials of different degrees: the DG solution polynomial on this tetrahedral cell and a sequence of hierarchical "modified" solution polynomials based on the L^2 projection methodology. The nonlinear weights in the convex combination coefficients follow the multi-resolution WENO procedure. For simplicity, we rewrite $u_h(x,y,z,t)$ to be $u_h(x,y,z)\in W_h^k=\{v(x,y,z):v(x,y,z)|_{\Delta_0}\in\mathbb{P}^k(\Delta_0)\}$ in the following, if it does not cause confusion. Now we assume Δ_0 is a troubled cell which is detected by our new three-dimensional troubled cell indicator. The procedure to reconstruct a new polynomial on the troubled cell Δ_0 by using the new multi-resolution WENO reconstruction procedure is summarized in the following:

Step 1.1. Define a series of polynomials of different degrees on the troubled cell Δ_0. The polynomials $q_\zeta(x,y,z)$, $\zeta=0,\cdots,k$ should satisfy the conditions that

$$\int_{\Delta_0} q_\zeta(x,y,z)v_l^{(0)}(x,y,z)dxdydz=\int_{\Delta_0} u_h(x,y,z)v_l^{(0)}(x,y,z)dxdydz,\quad l=0,\cdots,K_\zeta, \tag{3.2}$$

where $K_\zeta=\frac{(\zeta+1)(\zeta+2)(\zeta+3)}{6}-1$.

Remark 3.1. The construction of different polynomials $q_\zeta(x,y,z)$, $\zeta=0,\cdots,k$ is very simple, since the local orthonormal basis $v_l^{(0)}(x,y,z)$ is defined over Δ_0. In this case, we can directly obtain $q_\zeta(x,y,z)=\sum_{l=0}^{K_\zeta}u_0^{(l)}(t)v_l^{(0)}(x,y,z)$, $\zeta=0,\cdots,k$, respectively.

Step 1.2. Obtain equivalent expressions for these constructed polynomials of different degrees. To keep consistent notation, we will denote $p_{0,1}(x,y,z)=q_0(x,y,z)$. For different

high-order approximations, following original ideas for classical CWENO schemes [8,46, 47], we obtain polynomials $p_{\zeta,\zeta}(x,y,z)$, $\zeta=1,\cdots,k$ through

$$p_{\zeta,\zeta}(x,y,z)=\frac{1}{\gamma_{\zeta,\zeta}}q_{\zeta}(x,y,z)-\frac{\gamma_{\zeta-1,\zeta}}{\gamma_{\zeta,\zeta}}p_{\zeta-1,\zeta}(x,y,z),\quad \zeta=1,\cdots,k, \tag{3.3}$$

with $\gamma_{\zeta-1,\zeta}+\gamma_{\zeta,\zeta}=1$ and $\gamma_{\zeta,\zeta}\neq 0$, together with polynomials $p_{\zeta,\zeta+1}(x,y,z)$, $\zeta=1,\cdots,k-1$ through

$$p_{\zeta,\zeta+1}(x,y,z)=\omega_{\zeta,\zeta}p_{\zeta,\zeta}(x,y,z)+\omega_{\zeta-1,\zeta}p_{\zeta-1,\zeta}(x,y,z),\quad \zeta=1,\cdots,k-1, \tag{3.4}$$

with $\omega_{\zeta-1,\zeta}+\omega_{\zeta,\zeta}=1$. In these expressions, $\gamma_{\zeta-1,\zeta}$ and $\gamma_{\zeta,\zeta}$ are the linear weights, and $\omega_{\zeta-1,\zeta}$ and $\omega_{\zeta,\zeta}$ are the nonlinear weights (which will be precisely narrated later), respectively. Based on a balance between the sharp and essentially non-oscillatory shock transitions in non-smooth regions and accuracy in smooth regions, following the practice in [25,73,82], we set the linear weights as $\gamma_{\zeta-1,\zeta}=0.01$ and $\gamma_{\zeta,\zeta}=0.99$, $\zeta=1,\cdots,k$, respectively.

Step 1.3. Compute the smoothness indicators $\beta_{\zeta_2,\zeta}$, which measure how smooth the functions $p_{\zeta_2,\zeta}(x,y,z)$ for $\zeta_2=\zeta-1,\zeta$; $\zeta=1,\cdots,k$ are in the tetrahedral cell Δ_0. We use the same recipe for the smoothness indicators as in [41,65]:

$$\beta_{\zeta_2,\zeta}=\sum_{|\alpha|=1}^{\kappa}\int_{\Delta_0}\Delta_0^{|\alpha|-1}\left(\frac{\partial^{|\alpha|}}{\partial x^{\alpha_1}\partial y^{\alpha_2}\partial z^{\alpha_3}}p_{\zeta_2,\zeta}(x,y,z)\right)^2 dxdydz,\ \ \zeta_2=\zeta-1,\zeta;\ \ \zeta=1,\cdots,k, \tag{3.5}$$

where $\kappa=\zeta_2$, $\alpha=(\alpha_1,\alpha_2,\alpha_3)$, and $|\alpha|=\alpha_1+\alpha_2+\alpha_3$, respectively. The only exception is $\beta_{0,1}$, which we magnify from zero to a value defined below. Since Δ_ξ, $\xi=1,\cdots,4$ are denoted as the four neighboring tetrahedral cells of Δ_0, we first denote the linear polynomials $q_{0,\xi}(x,y,z)$ with the L^2 projection methodology of $u_h(x,y,z)\in W_h^k=\{v(x,y,z):v(x,y,z)|_{\Delta_\xi}\in \mathbb{P}^k(\Delta_\xi)\}$, $\xi=1,\cdots,4$, satisfying

$$\int_{\Delta_\xi}q_{0,\xi}(x,y,z)v_l^{(\xi)}(x,y,z)dxdydz=\int_{\Delta_\xi}u_h(x,y,z)v_l^{(\xi)}(x,y,z)dxdydz,$$
$$l=0,\cdots,3;\quad \xi=1,\cdots,4. \tag{3.6}$$

Remark 3.2. Since the local orthonormal bases $v_l^{(\xi)}(x,y,z)$ are defined over Δ_ξ, we can obtain $q_{0,\xi}(x,y,z)=\sum_{l=0}^{3}u_\xi^{(l)}(t)v_l^{(\xi)}(x,y,z)$, $\xi=1,\cdots,4$.

Then the associated smoothness indicators are

$$\theta_{0,\xi}=\int_{\Delta_0}\left(\frac{\partial}{\partial x}q_{0,\xi}(x,y,z)\right)^2+\left(\frac{\partial}{\partial y}q_{0,\xi}(x,y,z)\right)^2+\left(\frac{\partial}{\partial z}q_{0,\xi}(x,y,z)\right)^2 dxdydz,\quad \xi=1,\cdots,4. \tag{3.7}$$

After that, we define $\beta_{0,1}$ as

$$\beta_{0,1}=\min(\theta_{0,1},\theta_{0,2},\theta_{0,3},\theta_{0,4}). \tag{3.8}$$

Step 1.4. Compute the nonlinear weights based on the linear weights and the smoothness indicators. We adopt the WENO-Z recipe as shown in [4,9], with τ_ζ for $\zeta=1,\cdots,k$ defined as related to the absolute difference between the smoothness indicators:

$$\tau_\zeta=\left(\beta_{\zeta,\zeta}-\beta_{\zeta-1,\zeta}\right)^2,\quad \zeta=1,\cdots,k. \tag{3.9}$$

The nonlinear weights are then given as

$$\omega_{\zeta_2,\zeta}=\frac{\bar{\omega}_{\zeta_2,\zeta}}{\bar{\omega}_{\zeta-1,\zeta}+\bar{\omega}_{\zeta,\zeta}},\quad \bar{\omega}_{\zeta_2,\zeta}=\gamma_{\zeta_2,\zeta}\left(1+\frac{\tau_\zeta}{\varepsilon+\beta_{\zeta_2,\zeta}}\right),\quad \zeta_2=\zeta-1,\zeta;\ \ \zeta=1,\cdots,k. \tag{3.10}$$

Here ε is taken as 10^{-6} in all numerical simulations.

Step 1.5. The new final reconstruction polynomial on the troubled cell Δ_0 is given by

$$u_h^{new}|_{\Delta_0}=\sum_{\zeta_2=\zeta-1}^{\zeta}\omega_{\zeta_2,\zeta}p_{\zeta_2,\zeta}(x,y,z),\quad \zeta=1,\cdots,k, \tag{3.11}$$

for the second-order ($k=1$) and third-order ($k=2$) approximations.

Then the details of the new multi-resolution WENO limiting procedure are presented for the system case. Consider (1.1), where u, $f(u)$, $g(u)$, and $r(u)$ are vectors with five components. In order to keep the essentially non-oscillatory property, the multi-resolution WENO reconstruction limiter is used with a local characteristic field decompositions. In this paper, three-dimensional Euler equations are considered in the following

$$\frac{\partial}{\partial t}\begin{pmatrix}\rho\\ \rho\mu\\ \rho\nu\\ \rho w\\ E\end{pmatrix}+\frac{\partial}{\partial x}\begin{pmatrix}\rho\mu\\ \rho\mu^2+p\\ \rho\nu\mu\\ \rho w\mu\\ \mu(E+p)\end{pmatrix}+\frac{\partial}{\partial y}\begin{pmatrix}\rho\nu\\ \rho\mu\nu\\ \rho\nu^2+p\\ \rho w\nu\\ \nu(E+p)\end{pmatrix}+\frac{\partial}{\partial z}\begin{pmatrix}\rho w\\ \rho\mu w\\ \rho\nu w\\ \rho w^2+p\\ w(E+p)\end{pmatrix}=0, \tag{3.12}$$

where ρ is the density, μ is the x-direction velocity, ν is the y-direction velocity, w is the z-direction velocity, E is the total energy, p is the pressure, and $\gamma=1.4$ in the test cases. We denote the Jacobian matrices as $(f'(u),g'(u),r'(u))\cdot n_i$ and $n_i=(n_{ix},n_{iy},n_{iz})^T$, $i=1,\cdots,4$, are the outward unit normals to different triangular faces of the tetrahedral cell. The left and right eigenvector matrices of such Jacobian matrices are specified in [75]. Assuming $\triangle_0$ is the troubled cell detected by the new modified version of the original KXRCF technique [42], we denote associated polynomial vectors p_l^ξ (each of them is a 5-component vector with each component being an l-th degree polynomial, which is one of a sequence of hierarchical "modified" solution polynomials based on the L^2 projection

methodology), $l=0,\cdots,k$ on the troubled cell and its neighboring four tetrahedral cells (Δ_ξ, $\xi=0,\cdots,4$, respectively). We then perform the new multi-resolution WENO limiting procedure as follows:

Step 2.1. In each n_i-direction among four normal directions of $\partial\triangle_0$, we reconstruct new polynomial vectors p_i^{new}, $i=1,\cdots,4$ by using the characteristic-wise new multi-resolution WENO limiting procedure with the associated Jacobian $f'(u)n_{ix}+g'(u)n_{iy}+r'(u)n_{iz}$, $i=1,\cdots,4$ as specified in [75]:

Step 2.1.1. Project the polynomial vectors p_l^ξ into the characteristic fields $\tilde{p}_{i_l}^\xi = L_i \cdot p_l^\xi$, and $\tilde{p}_{i_l}^\xi$, $i=1,\cdots,4$; $l=0,\cdots,k$; and $\xi=0,\cdots,4$, respectively.

Step 2.1.2. For each component, we perform Step 1.1 to Step 1.5 of the new multi-resolution WENO limiting procedure that has been specified for the scalar case, to obtain the new 5-component vectors on the troubled cell $\triangle_0$ as $\tilde{p}_i^{new}$, $i=1,\cdots,4$, respectively.

Step 2.1.3. Project $\tilde{p}_i^{new}$ into the physical space $p_i^{new}=R_i\cdot\tilde{p}_i^{new}$, $i=1,\cdots,4$.

Step 2.2. The final new 5-component vector on the troubled cell $\triangle_0$ is defined as

$$u_h^{new}|_{\Delta_0}=\frac{\sum_{i=1}^4 p_i^{new}|\triangle_i|}{\sum_{i=1}^4|\triangle_i|}.$$

4 Numerical results

In this section, some benchmark numerical results are applied to demonstrate the good performance of the new three-dimensional multi-resolution WENO reconstructions as limiters for the RKDG methods on tetrahedral meshes described before. The time step is chosen according to the CFL condition

$$\Delta t \max_{1\le i\le N}\left(\frac{\sum_{\ell\hat{\ell}=1}^4(|(\mu_i,\nu_i,w_i)\cdot n_{i_{\ell\ell}}|+c_i)|\partial\Delta_{i_{\ell\ell}}|}{|\Delta_i|}\right)\le \text{CFL},$$

where $c_i=\sqrt{\frac{\gamma p_i}{\rho_i}}$ is the sound speed with $\gamma=1.4$. The CFL number is 0.3 for the second-order (P^1) and 0.18 for the third-order (P^2) RKDG methods [17] with and without the new multi-resolution WENO limiters on tetrahedral meshes. We perform the new multi-resolution WENO limiting procedure on every tetrahedral cell (that is, we artificially declare all cells to be troubled cells) for solving all the accuracy tests, in order to fully testify the influence of the limiter upon accuracy. To be more specific, we define all tetrahedral cells as troubled cells in Example 4.1, Example 4.2, and Example 4.3, and we will set the constant $C_k=1$ in (3.1) for other examples, unless specified otherwise. The linear weights are set as $\gamma_{\zeta-1,\zeta}$=0.01 and $\gamma_{\zeta,\zeta}$=0.99, $\zeta=1,2$, for simplicity in this paper.

Example 4.1. The linear scalar equation

$$\mu_t+\mu_x+\mu_y+\mu_z=0, \tag{4.1}$$

is considered in the computational domain $[-2,2]\times[-2,2]\times[-2,2]$ on the uniform tetrahedral meshes. The initial condition is $\mu(x,y,z,0)=\sin(\pi(x+y+z)/2)$ and periodic boundary conditions are applied in all three directions. The final time is $t=1$. The errors and numerical orders of accuracy for the RKDG methods with multi-resolution WENO limiters comparing with the original RKDG methods without limiters are shown in Table 1. The numerical error against CPU time graphs for the RKDG methods with and without the multi-resolution WENO limiters are shown in Fig. 1 for a comparison. We can see that the new multi-resolution WENO limiters can keep the designed order of accuracy, although the magnitude of the errors is bigger than that of the original RKDG methods on the same mesh, especially for the coarser meshes.

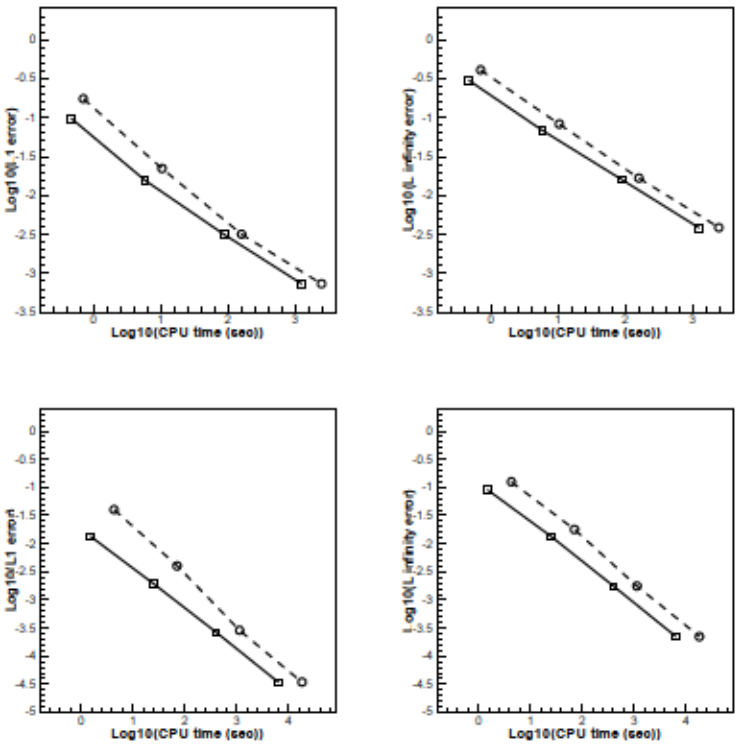

Figure 1: The linear scalar equation. $T=1$. Computing time and error. Squares and a solid line: the results of RKDG methods without multi-resolution WENO limiters; circles and a dashed line: the results of RKDG methods with multi-resolution WENO limiters. From left to right: L^1 error; L^∞ error. From top to bottom: second-order (P^1); third-order (P^2).

Table 1: $\mu_t+\mu_x+\mu_y+\mu_z=0$. $\mu(x,y,z,0)=\sin(\pi(x+y+z)/2)$. Periodic boundary conditions in three directions. $T=1$. L^1 and L^∞ errors. RKDG with/without WENO limiter. Uniform tetrahedral mesh.

		RKDG with WENO limiter				RKDG without WENO limiter			
	tetrahedrons	L^1 error	order	L^∞ error	order	L^1 error	order	L^∞ error	order
P^1	750	1.73E-1		4.06E-1		9.76E-2		2.98E-1	
	6000	2.22E-2	2.97	8.24E-2	2.30	1.55E-2	2.65	6.82E-2	2.13
	48000	3.17E-3	2.81	1.67E-2	2.30	3.15E-3	2.30	1.60E-2	2.09
	384000	7.35E-4	2.11	3.98E-3	2.07	7.34E-4	2.10	3.84E-3	2.06
P^2	750	3.99E-2		1.24E-1		1.33E-2		8.94E-2	
	6000	4.00E-3	3.32	1.77E-2	2.81	1.92E-3	2.79	1.33E-2	2.74
	48000	2.86E-4	3.80	1.75E-3	3.34	2.63E-4	2.87	1.74E-3	2.94
	384000	3.44E-5	3.06	2.21E-4	2.99	3.43E-5	2.94	2.21E-4	2.98

Example 4.2. The following nonlinear scalar Burgers' equation

$$\mu_t+\left(\frac{\mu^2}{2}\right)_x+\left(\frac{\mu^2}{2}\right)_y+\left(\frac{\mu^2}{2}\right)_z=0, \tag{4.2}$$

is considered in the computational domain $[-3,3]\times[-3,3]\times[-3,3]$ on the uniform tetrahedral meshes. The initial condition is $\mu(x,y,z,0)=0.5+\sin(\pi(x+y+z)/3)$ and periodic boundary conditions are applied in all three directions. The final time is $t=0.5/\pi^2$, when the solution is still smooth. The errors and numerical orders of accuracy for the RKDG methods with the new multi-resolution WENO limiters comparing with the original RKDG methods without the multi-resolution WENO limiters are shown in Table 2. The numerical errors against CPU time graphs for the RKDG methods with and without the multi-resolution WENO limiters are shown in Fig. 2 for a comparison. We can also see

Table 2: $\mu_t+(\frac{\mu^2}{2})_x+(\frac{\mu^2}{2})_y+(\frac{\mu^2}{2})_z=0$. $\mu(x,y,z,0)=0.5+\sin(\pi(x+y+z)/3)$. Periodic boundary conditions in three directions. $T=0.5/\pi^2$. L^1 and L^∞ errors. RKDG with/without limiter. Uniform tetrahedral mesh.

		RKDG with WENO limiter				RKDG without limiter			
	tetrahedrons	L^1 error	order	L^∞ error	order	L^1 error	order	L^∞ error	order
P^1	750	3.31E-2		1.38E-1		3.32E-2		1.40E-1	
	6000	1.43E-2	1.21	5.08E-2	1.45	1.08E-2	1.61	5.07E-2	1.47
	48000	3.22E-3	2.15	1.47E-2	1.79	3.23E-3	1.75	1.49E-2	1.77
	384000	8.51E-4	1.92	4.24E-3	1.79	8.50E-4	1.93	3.94E-3	1.92
P^2	750	1.28E-2		9.64E-2		7.63E-3		7.82E-2	
	6000	1.50E-3	3.09	1.24E-2	2.96	1.12E-3	2.76	1.23E-2	2.66
	48000	1.69E-4	3.15	2.02E-3	2.62	1.66E-4	2.76	2.02E-3	2.61
	384000	2.46E-5	2.78	3.04E-4	2.73	2.46E-5	2.75	3.04E-4	2.73

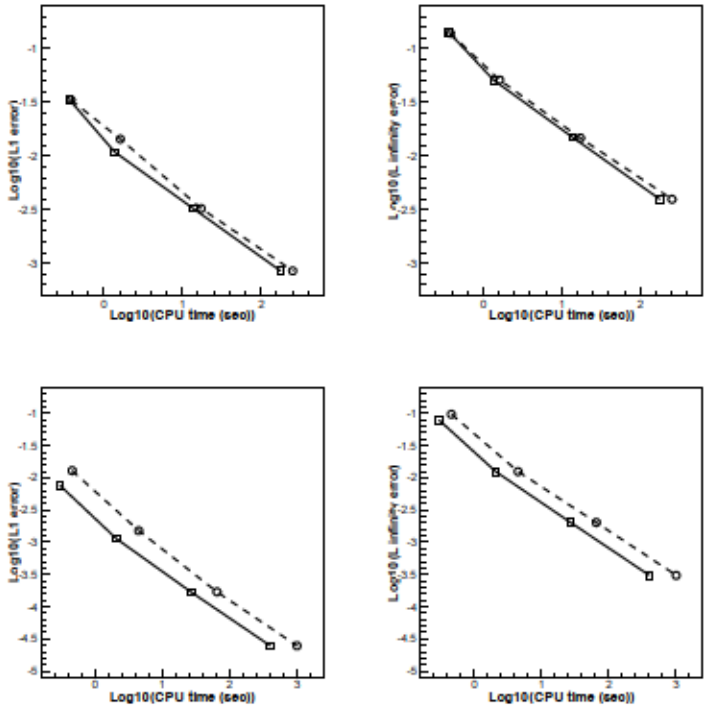

Figure 2: The Burgers' equation. $T=\frac{0.5}{\pi}$. Computing time and error. Squares and a solid line: the results of RKDG methods without multi-resolution WENO limiters; circles and a dashed line: the results of RKDG methods with multi-resolution WENO limiters. From left to right: L^1 error; L^∞ error. From top to bottom: second-order (P^1); third-order (P^2).

that the new multi-resolution WENO limiters could keep the designed order of accuracy, however the magnitude of the errors is larger than that of the original RKDG methods without limiters on the same mesh, especially for coarser meshes.

Example 4.3. We solve three-dimensional Euler equations (3.12). The initial conditions are: $\rho(x,y,z,0)=1+0.9\sin(\pi(x+y+z)/3)$, $\mu(x,y,z,0)=3$, $\nu(x,y,z,0)=3$, $w(x,y,z,0)=3$, and $p(x,y,z,0)=1$. The computational domain is $[0,6]\times[0,6]\times[0,6]$ on the uniform tetrahedral meshes and the periodic boundary conditions are applied in all three directions. The final time is $t=1$. The errors and numerical orders of accuracy of the density for the RKDG methods with the new multi-resolution WENO limiters comparing with the original RKDG methods without limiters are shown in Table 3. The numerical errors against CPU time graphs for the RKDG methods with and without the multi-resolution WENO limiters are shown in Fig. 3 for a comparison. Similar to the previous example, we can see that the new multi-resolution WENO limiters can again keep the designed order of

Table 3: 3D-Euler equations: initial data $\rho(x,y,z,0)=1+0.9\sin(\pi(x+y+z)/3)$, $\mu(x,y,z,0)=3$, $\nu(x,y,z,0)=3$, $w(x,y,z,0)=3$, and $p(x,y,z,0)=1$. Periodic boundary conditions in three directions, $T=1$. L^1 and L^∞ errors. RKDG with/without limiter. Uniform tetrahedral mesh.

		RKDG with WENO limiter				RKDG without limiter			
	tetrahedrons	L^1 error	order	L^∞ error	order	L^1 error	order	L^∞ error	order
P^1	750	2.87E-1		5.37E-1		1.61E-1		3.71E-1	
	6000	4.56E-2	2.65	1.28E-1	2.06	1.92E-2	3.07	6.48E-2	2.52
	20250	1.22E-2	3.24	4.38E-2	2.65	6.78E-3	2.57	2.67E-2	2.18
	48000	4.07E-3	3.83	1.88E-2	2.92	3.51E-3	2.29	1.44E-2	2.15
P^2	750	6.14E-2		1.97E-1		2.31E-2		1.14E-1	
	6000	6.88E-3	3.16	3.06E-2	2.69	3.74E-3	2.63	1.87E-2	2.61
	20250	1.51E-3	3.73	8.37E-3	3.20	1.24E-3	2.72	6.11E-3	2.77
	48000	5.70E-4	3.39	3.16E-3	3.38	5.54E-4	2.80	2.71E-3	2.82

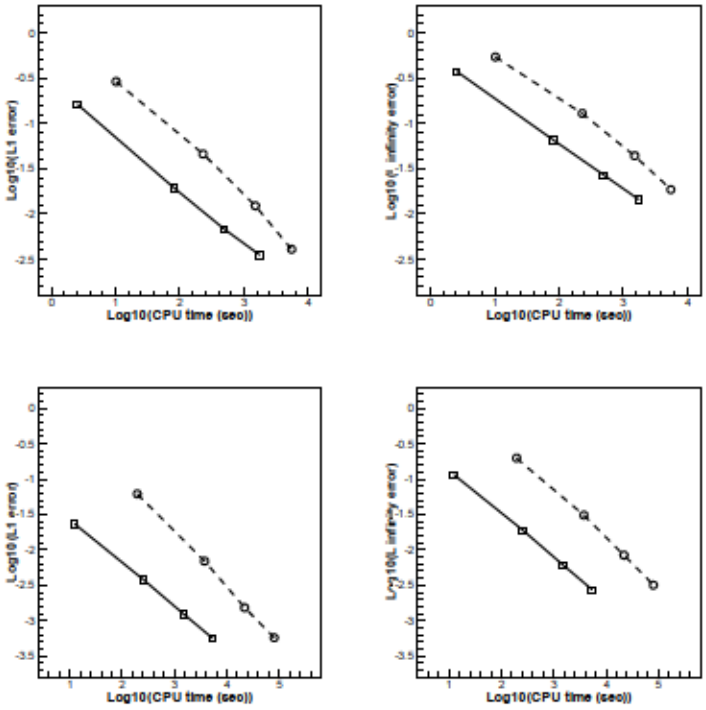

Figure 3: 3D-Euler equations. $T=1$. Computing time and error. Squares and a solid line: the results of RKDG methods without multi-resolution WENO limiters; circles and a dashed line: the results of RKDG methods with multi-resolution WENO limiters. From left to right: L^1 error; L^∞ error. From top to bottom: second-order (P^1); third-order (P^2).

accuracy, with the magnitude of the errors larger than that of the original RKDG methods on the same mesh.

Example 4.4. We solve the three-dimensional Euler equations (3.12) with the Riemann initial condition for the Lax problem [44]:

$$(\rho,\mu,\nu,w,p,\gamma)^T \tag{4.3}$$
$$=\begin{cases} (0.445,0.698,0,0,3.528,1.4)^T, & (x,y,z)^T\in[-0.5,0)\times[-0.02,0.02]\times[-0.02,0.02], \\ (0.5,0,0,0,0.571,1.4)^T, & (x,y,z)^T\in[0,0.5]\times[-0.02,0.02]\times[-0.02,0.02]. \end{cases}$$

The new multi-resolution WENO limiters are applied to this one-dimensional shock tube problem. The solution lies in the domain of $[-0.5,0.5]\times[-0.02,0.02]\times[-0.02,0.02]$ with a tetrahedralization of 101 vertices in the x-direction and 5 vertices in the y-direction and z-direction, respectively. The velocities in the y-direction and z-direction are set as 0 and periodic boundary conditions are applied in these directions. The final time is t=0.16. We present the exact solution and the computed density ρ obtained by the RKDG methods with the new multi-resolution WENO limiters in Fig. 4.

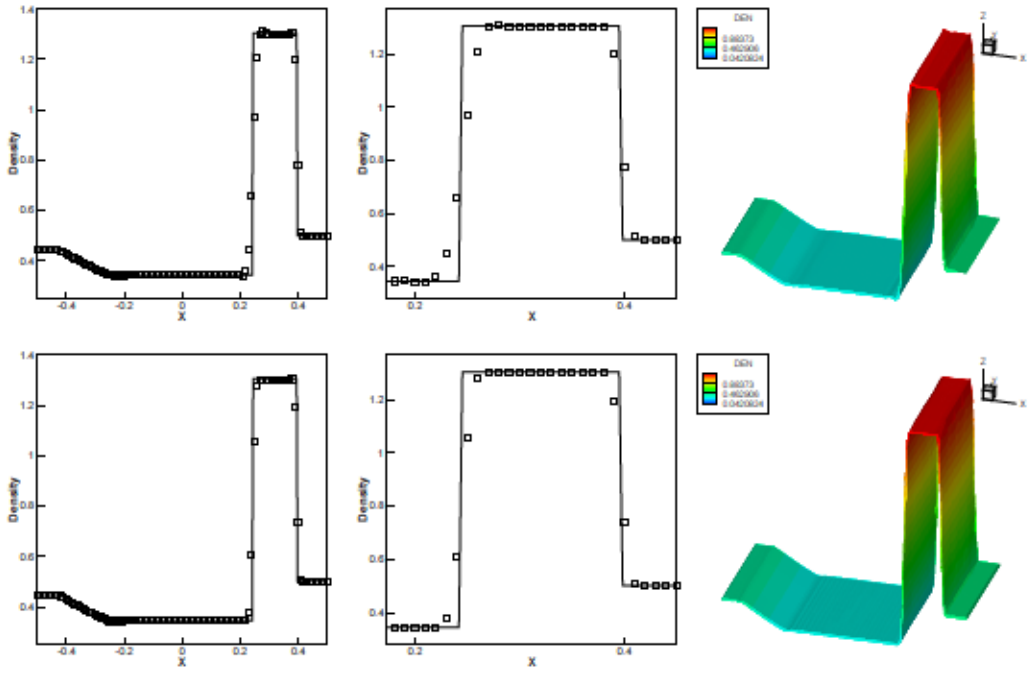

Figure 4: The Lax problem. $T=0.16$. From top to bottom: second-order (P^1); third-order (P^2). From left to right: density cutting-plot along $y=z=0$; density zoomed in; density surface cutting-plot along $z=0$. Solid line: exact solution; squares: RKDG methods with multi-resolution WENO limiters. The mesh points on the boundary are uniformly distributed with cell length $\Delta x=\Delta y=\Delta z=1/100$.

Example 4.5. We solve the three-dimensional Euler equations (3.12) with the Riemann initial condition for the Sod problem [67]:

$$\begin{aligned}&(\rho,\mu,\nu,w,p,\gamma)^T\\&=\begin{cases}(1,0,0,0,2.5,1.4)^T, & (x,y,z)^T\in[-5,0)\times[-0.2,0.2]\times[-0.2,0.2],\\(0.125,0,0,0,0.25,1.4)^T, & (x,y,z)^T\in[0,5]\times[-0.2,0.2]\times[-0.2,0.2].\end{cases}\end{aligned}\tag{4.4}$$

The solution lies in the domain of $[-5,5]\times[-0.2,0.2]\times[-0.2,0.2]$ with a tetrahedralization of 101 vertices in the x-direction and 5 vertices in the y-direction and z-direction, respectively. The velocities in the y-direction and z-direction are set as 0 and periodic boundary conditions are applied in these directions. The final time is $t=2$. We present the exact solution and the computed density ρ obtained by the RKDG methods with the new multi-resolution WENO limiters, and the RKDG methods with TVB limiter, TVB constant $M=1$ [17] in Fig. 5 for a comparison. The numerical results computed by using the new multi-resolution WENO limiters are good for this test case.

Example 4.6. A higher order scheme would show its advantage when the solution contains both shocks and complex smooth region structures. A typical example for this is the problem of shock interaction with entropy waves [63]. We solve three-dimensional Euler equations (3.12) with a moving Mach number 3 shock interacting with sine waves in density: $(\rho,\mu,\nu,w,p,\gamma)^T=(3.857143,2.629369,0,0,10.333333,1.4)^T$ for $(x,y,z)^T\in[-5,-4)\times[-0.1,0.1]\times[-0.1,0.1]$; $(\rho,\mu,\nu,w,p,\gamma)^T=(1+0.2\sin(5x),0,0,0,1,1.4)^T$ for $(x,y,z)^T\in[-4,5]\times[-0.1,0.1]\times[-0.1,0.1]$. The solution lies in the computational domain $[-5,5]\times[-0.1,0.1]\times[-0.1,0.1]$ with a tetrahedralization of 201 vertices in the x-direction and 5 vertices in the y-direction and z-direction, respectively. The velocities in the y-direction and z-direction are set as 0 and periodic boundary conditions are applied in these directions. The computed density ρ is plotted at $t=1.8$ against the reference "exact" solution which is a converged solution computed by the one-dimensional fifth-order finite difference WENO scheme [41] with 2000 grid points in Fig. 4. We also present the RKDG methods with TVB limiter, TVB constant $M=1$ [17] in Fig. 4 for a comparison. The second-order and third-order RKDG methods with the new multi-resolution WENO limiters could get good resolution for this benchmark example.

Example 4.7. We now consider the interaction of two blast waves [71]. The initial conditions are

$$\begin{aligned}&(\rho,\mu,\nu,w,p,\gamma)^T\\&=\begin{cases}(1,0,0,0,10^3,1.4)^T, & (x,y,z)^T\in[0,0.1]\times[-0.005,0.005]\times[-0.005,0.005],\\(1,0,0,0,10^{-2},1.4)^T, & (x,y,z)^T\in(0.1,0.9]\times[-0.005,0.005]\times[-0.005,0.005],\\(1,0,0,0,10^2,1.4)^T, & (x,y,z)^T\in(0.9,1]\times[-0.005,0.005]\times[-0.005,0.005].\end{cases}\end{aligned}\tag{4.5}$$

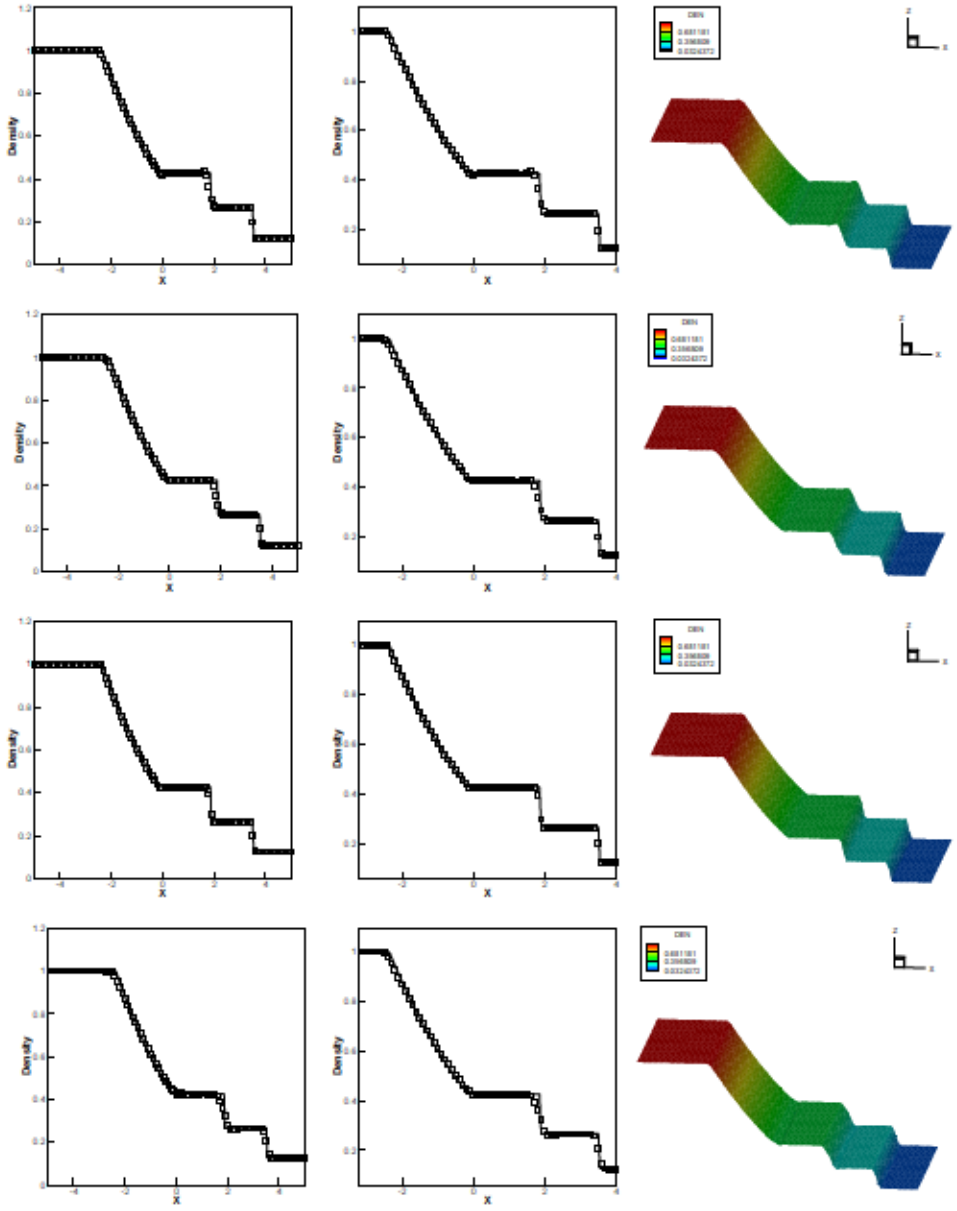

Figure 5: The Sod problem. $T=2$. From top to bottom: second-order (P^1), RKDG methods with multi-resolution WENO limiters; second-order (P^1), RKDG methods with TVB limiter, TVB constant $M=1$; third-order (P^2), RKDG methods with multi-resolution WENO limiters; third-order (P^2), RKDG methods with TVB limiter, TVB constant $M=1$. From left to right: density cutting-plot along $y=z=0$; density zoomed in; density surface cutting-plot along $z=0$. Solid line: exact solution; squares: RKDG methods with limiters. The mesh points on the boundary are uniformly distributed with cell length $\Delta x=\Delta y=\Delta z=10/100$.

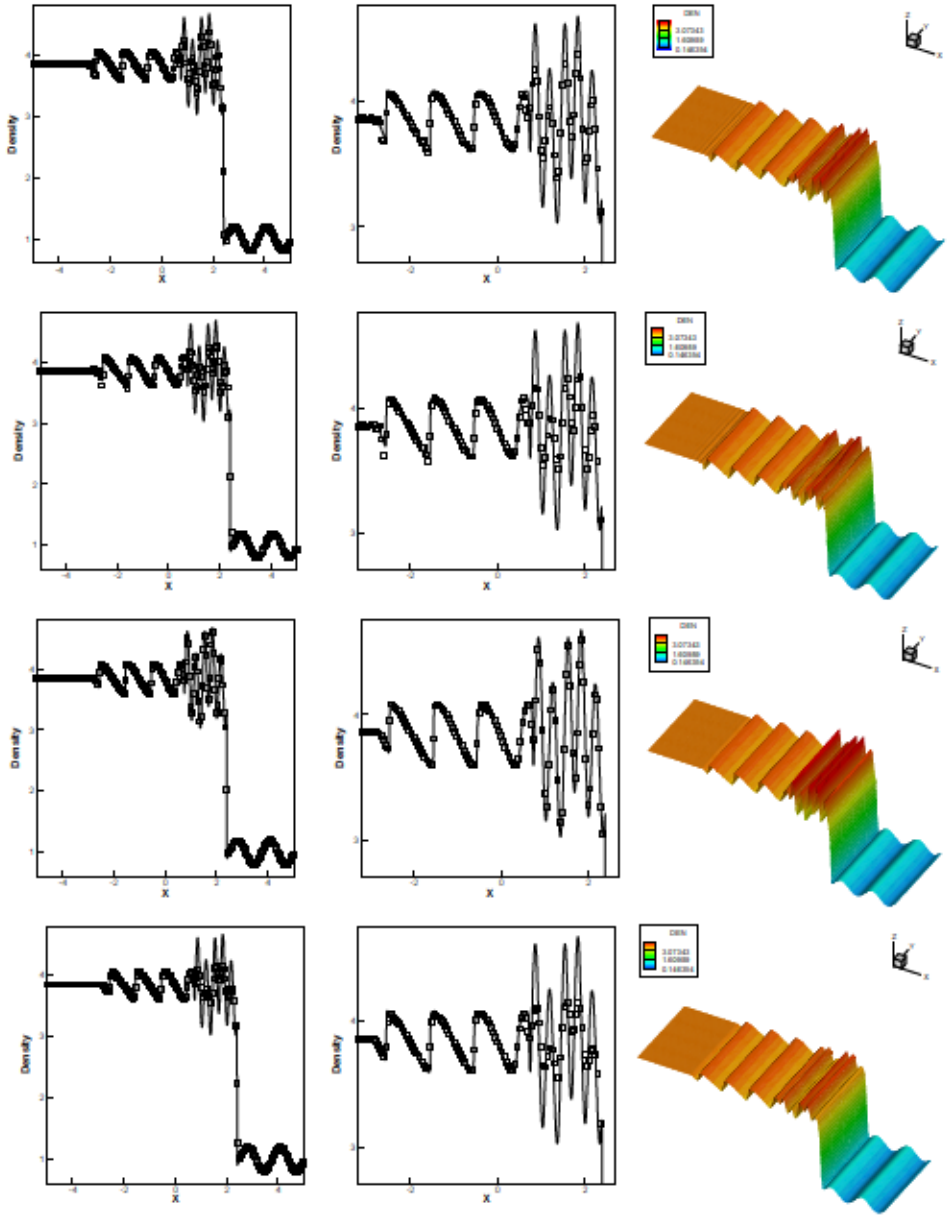

Figure 6: The shock density wave interaction problem. $T=1.8$. From top to bottom: second-order (P^1), RKDG methods with multi-resolution WENO limiters; second-order (P^1), RKDG methods with TVB limiter, TVB constant $M=1$; third-order (P^2), RKDG methods with multi-resolution WENO limiters; third-order (P^2), RKDG methods with TVB limiter, TVB constant $M=1$. From left to right: density cutting-plot along $y=z=0$; density zoomed in; density surface cutting-plot along $z=0$. Solid line: reference "exact" solution; squares: RKDG methods with limiters. The mesh points on the boundary are uniformly distributed with cell length $\Delta x=\Delta y=\Delta z=10/200$.

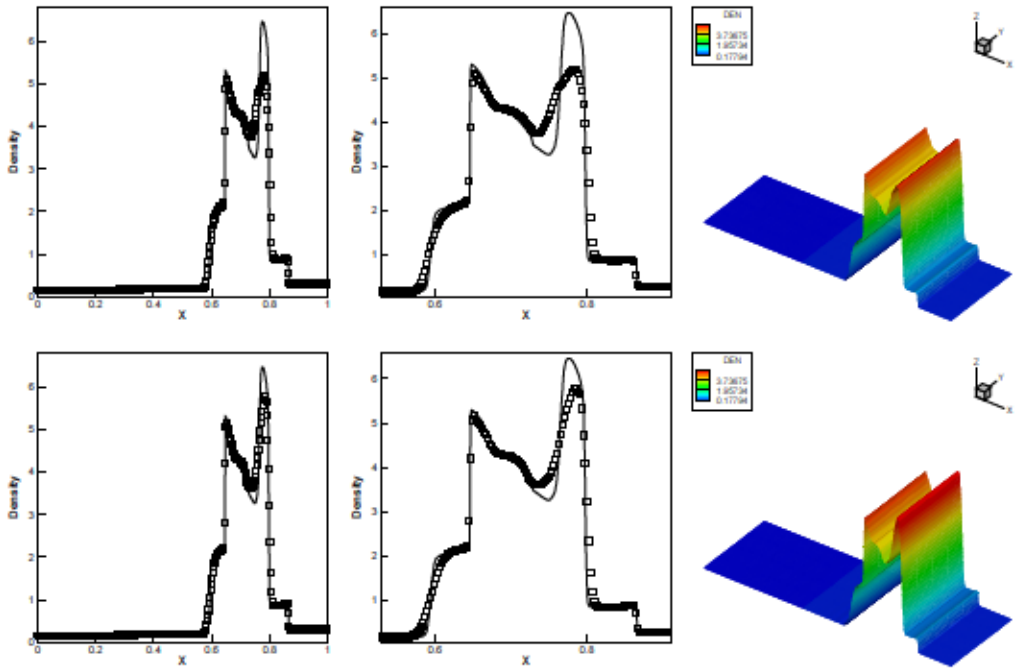

Figure 7: The blast wave problem. $T=0.038$. From top to bottom: second-order (P^1); third-order (P^2). From left to right: density cutting-plot along $y=z=0$; density zoomed in; density surface cutting-plot along $z=0$. Solid line: exact solution; squares: RKDG methods with multi-resolution WENO limiters. The mesh points on the boundary are uniformly distributed with cell length $\Delta x=\Delta y=\Delta z=1/400$.

The solution of three-dimensional Euler equations (3.12) lies in the domain of $[0,1]\times[-0.005,0.005]\times[-0.005,0.005]$ with a tetrahedralization of 401 vertices in the x-direction and 5 vertices in the y-direction and z-direction, respectively. The velocities in the y-direction and z-direction are set as 0 and periodic boundary conditions are applied in these directions. The computed density ρ is plotted at $t=0.038$ against the reference "exact" solution which is a converged solution computed by the one-dimensional fifth-order finite difference WENO scheme [41] with 2000 grid points in Fig. 7. The RKDG methods with the new multi-resolution WENO limiters could get good performance once again.

Example 4.8. We solve the same nonlinear Burgers' equation (4.2) with the same initial condition $\mu(x,y,z,0)=0.5+\sin(\pi(x+y+z)/3)$, except that the results are plotted at $t=5/\pi^2$, when a shock has already appeared in the solution. In Fig. 8, we show the contours on the surface and one dimensional cutting-plot along $x=y$, $z=0$ of the solutions by the second-order and third-order RKDG methods with the new multi-resolution WENO limiters. We can see that the new schemes give non-oscillatory shock transitions for this problem.

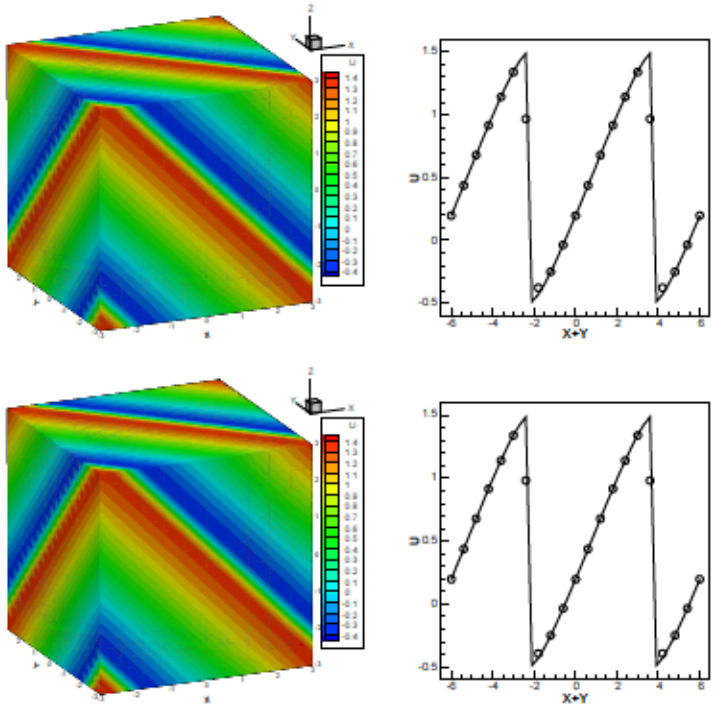

Figure 8: Burgers' equation. $T=5/\pi^2$. From top to bottom: second-order (P^1); third-order (P^2). From left to right: contour plot on the surface; 1D cutting-plot along $x=y$, $z=0$ with circles representing the numerical solution of RKDG methods with multi-resolution WENO limiters and the line representing the exact solution. The mesh points on the boundary are uniformly distributed with cell length $\Delta x=\Delta y=\Delta z=6/20$.

Example 4.9. We use INRIA's 3D tetrahedral elements for the BTC0 (streamlined body, laminar) test case [43] in project ADIGMA with the initial conditions: the Mach number $M_\infty=0.5$ and angle of attack $\alpha=0°$. The computational domain is $\sqrt{x^2+y^2+z^2}\leq 10$ which consists of 191753 tetrahedrons and 33708 points with 8244 triangles over the surface. The surface mesh used in the computation is shown in Fig. 9. The second-order and third-order RKDG methods with the new multi-resolution WENO limiters are used in this numerical test. Density plotted on the surface with 80 equally spaced contours from 0.98 to 1.13 and pressure plotted on the surface with 80 equally spaced contours from 0.97 to 1.19 are shown in Fig. 10. We can also see that two schemes can perform well with good resolution.

Example 4.10. We consider inviscid Euler transonic flow past a single Y3815-pb11 plane (the repository of this free 3D model is available at INRIA's Free 3D Meshes Download http://www-rocq1.inria.fr/gamma) with Mach number $M_\infty=0.8$ and angle of attack $\alpha=1.25°$. The computational domain is $\sqrt{x^2+y^2+z^2}\leq 100$ which consists of 180855 tetrahedrons and 50588 points with 24640 triangles over the surface. The surface mesh used in

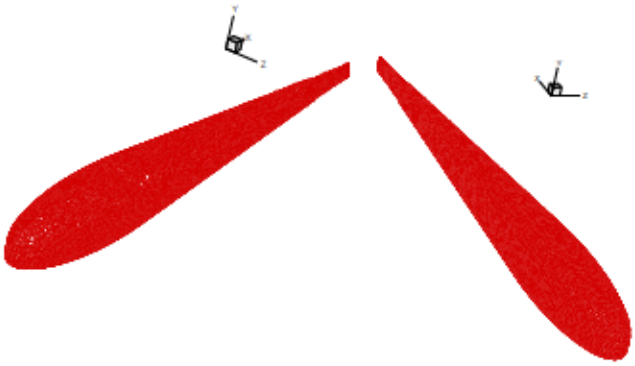

Figure 9: BTC0 surface mesh, zoomed in.

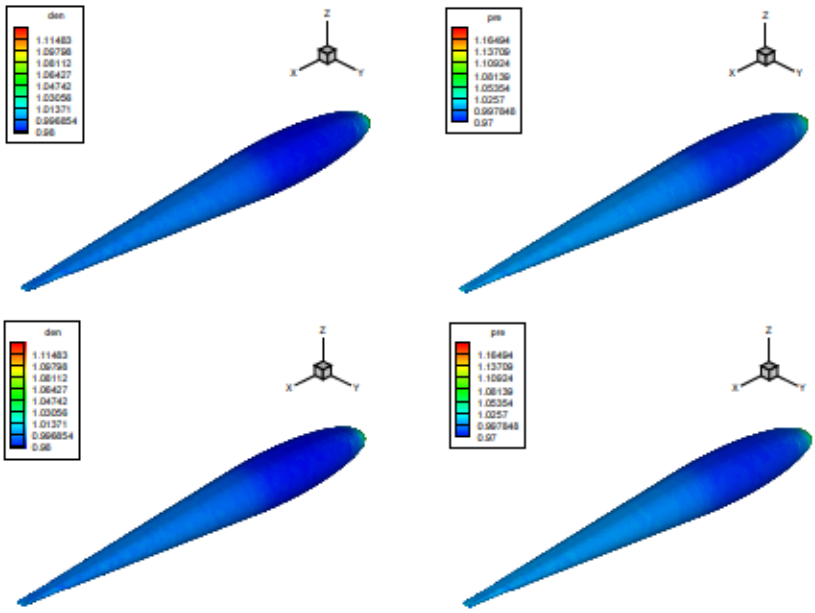

Figure 10: BTC0 problem. $M_\infty = 0.5$ and angle of attack $\alpha = 0°$. From top to bottom: second-order (P^1); third-order (P^2). From left to right: density plotted on the surface with 80 equally spaced contours from 0.98 to 1.13; pressure plotted on the surface with 80 equally spaced contours from 0.97 to 1.19.

the computation is shown in Fig. 11. The second-order and third-order RKDG methods with new multi-resolution WENO limiters are used in this benchmark numerical test. Density plotted on the Y3815-pb1l plane with 80 equally spaced contours from 0.09 to 1.32 and pressure plotted on the Y3815-pb1l plane with 80 equally spaced contours from 0.06 to 1.53 are shown in Fig. 12. We can see that the second-order and third-order RKDG methods with multi-resolution WENO limiters perform well with good resolution.

Figure 11: Y3815-pb1l plane surface mesh, zoomed in.

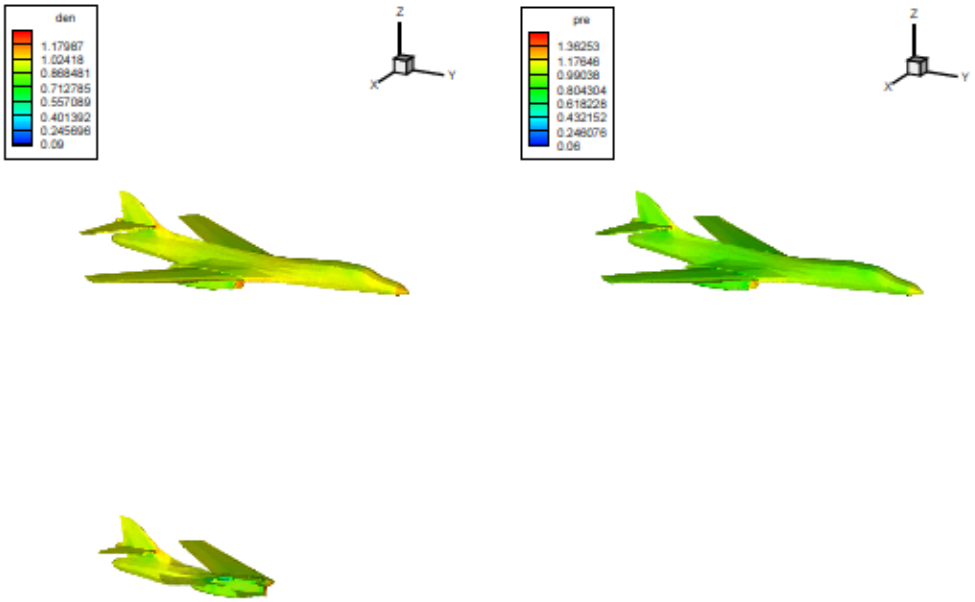

the RKDG methods is to apply a new three-dimensional modified version of the original KXRCF shock detection technique [42] to detect troubled cells subject to the multi-resolution WENO limiting procedures on tetrahedral meshes, and to construct a sequence of hierarchical L^2 projection polynomial solutions of the DG methods over the tetrahedral troubled cells. The main innovation is the new multi-resolution WENO reconstruction procedures, which basically only use the information defined within the tetrahedral troubled cell, with information from neighboring four tetrahedral cells used marginally in the determination of the smoothness indicator of the zeroth degree polynomial in the hierarchy, and with simple positive linear weights in the spatial reconstruction procedures. This new spatial reconstruction methodology is simpler, more robust, and could lead to better resolutions for some benchmark numerical examples than previous WENO type limiters that applied for high-order RKDG methods on tetrahedral meshes.

Acknowledgments

The first author was supported by NSFC grant 11872210 and Science Challenge Project, No. TZ2016002. And the first author was also partly supported by NSFC grant 11926103 when he visited Tianyuan Mathematical Center in Southeast China, Xiamen, Fujian 361005, P.R. China. The second author was supported by AFOSR grant FA9550-20-1-0055 and NSF grants DMS-1719410 and DMS-2010107. The third author was supported by NSAF grant U1630247 and Science Challenge Project, No. TZ2016002.

References

[1] D. Balsara, C. Altmann, C.D. Munz and M. Dumbser, A sub-cell based indicator for troubled zones in RKDG schemes and a novel class of hybrid RKDG+HWENO schemes, J. Comput. Phys., 226 (2007), 586-620.

[2] L. Bao, R.D. Nair and H.M. Tufo, A mass and momentum flux-form high-order discontinuous Galerkin shallow water model on the cubed-sphere, J. Comput. Phys., 271 (2014), 224-243.

[3] R. Biswas, K.D. Devine and J. Flaherty, Parallel, adaptive finite element methods for conservation laws, Appl. Numer. Math., 14 (1994), 255-283.

[4] R. Borges, M. Carmona, B. Costa and W.S. Don, An improved weighted essentially non-oscillatory scheme for hyperbolic conservation laws, J. Comput. Phys., 227 (2008), 3191-3211.

[5] W. Boscheri, D.S. Balsara, High order direct Arbitrary-Lagrangian-Eulerian (ALE) PNPM schemes with WENO adaptive-order reconstruction on unstructured meshes, J. Comput. Phys., 398 (2019), 108899.

[6] W. Boscheri, M. Semplice and M. Dumbser, Central WENO subcell finite volume limiters for ADER discontinuous Galerkin schemes on fixed and moving unstructured meshes, Commun. Comput. Phys., 25 (2019), 311-346.

[7] A. Burbeau, P. Sagaut and C.H. Bruneau, A problem-independent limiter for high-order Runge-Kutta discontinuous Galerkin methods, J. Comput. Phys., 169 (2001), 111-150.

[8] G. Capdeville, A central WENO scheme for solving hyperbolic conservation laws on non-uniform meshes, J. Comput. Phys., 227 (2008), 2977-3014.

[9] M. Castro, B. Costa and W.S. Don, High order weighted essentially non-oscillatory WENO-Z schemes for hyperbolic conservation laws, J. Comput. Phys., 230 (2011), 1766-1792.
[10] J. Cheng, T. Liu and H. Luo, A hybrid reconstructed discontinuous Galerkin method for compressible flows on arbitrary grids, Comput. Fluids, 139 (2016), 68-79.
[11] J. Cheng, F. Zhang and T. Liu, A high order compact least-squares reconstructed discontinuous Galerkin method for the steady-state compressible flows on hybrid grids, J. Comput. Phys., 362 (2018), 95-113.
[12] B. Cockburn, Discontinuous Galerkin methods for convection-dominated problems, in T. Barth and H. Deconinck, editors, High-Order Methods for Computational Physics, Volume 9 of Lecture Notes in Computational Science and Engineering, Springer, Berlin, 1999, 69-224.
[13] B. Cockburn, S. Hou and C.-W. Shu, The Runge-Kutta local projection discontinuous Galerkin finite element method for conservation laws IV: the multidimensional case, Mathematics of Computation, 54 (1990), 545-581.
[14] B. Cockburn, S.-Y. Lin and C.-W. Shu, TVB Runge-Kutta local projection discontinuous Galerkin finite element method for conservation laws III: one dimensional systems, J. Comput. Phys., 84 (1989), 90-113.
[15] B. Cockburn and C.-W. Shu, TVB Runge-Kutta local projection discontinuous Galerkin finite element method for conservation laws II: general framework, Mathematics of Computation, 52 (1989), 411-435.
[16] B. Cockburn and C.-W. Shu, The Runge-Kutta local projection P1-discontinuous Galerkin finite element method for scalar conservation laws, RAIRO Model. Math. Anal. Numer., 25 (1991), 337-361.
[17] B. Cockburn and C.-W. Shu, The Runge-Kutta discontinuous Galerkin method for conservation laws V: multidimensional systems, J. Comput. Phys., 141 (1998), 199-224.
[18] B. Cockburn and C.-W. Shu, Runge-Kutta discontinuous Galerkin method for convection-dominated problems, J. Sci. Comput., 16 (2001), 173-261.
[19] I. Cravero, G. Puppo, M. Semplice and G. Visconti, CWENO: uniformly accurate reconstructions for balance laws, Math. Comput., 87 (2018), 1689-1719.
[20] I. Cravero and M. Semplice, On the accuracy of WENO and CWENO reconstructions of third order on nonuniform meshes, J. Sci. Comput., 67 (2016), 1219-1246.
[21] M. Dumbser, Arbitrary High Order Schemes for the Solution of Hyperbolic Conservation Laws in Complex Domains, Shaker Verlag, Aachen, 2005.
[22] M. Dumbser, D. Balsara, E.F. Toro and C.D. Munz, A unified framework for the construction of one-step finite-volume and discontinuous Galerkin schemes, J. Comput. Phys., 227 (2008), 8209-8253.
[23] M. Dumbser, W. Boscheri, M. Semplice and G. Russo, Central WENO schemes for hyperbolic conservation laws on fixed and moving unstructured meshes, SIAM J. Sci. Comput., 39 (2017), A2564-A2591.
[24] M. Dumbser, C. Enaux and E.F. Toro, Finite volume schemes of very high order of accuracy for stiff hyperbolic balance laws, J. Comput. Phys., 227 (2008), 3971-4001.
[25] M. Dumbser and M. Käser, Arbitrary high order non-oscillatory finite volume schemes on unstructured meshes for linear hyperbolic systems, J. Comput. Phys., 221 (2007), 693-723.
[26] M. Dumbser, M. Käeser, V.A. Titarev and E.F. Toro, Quadrature-free non-oscillatory finite volume schemes on unstructured meshes for nonlinear hyperbolic systems, J. Comput. Phys., 226 (2007), 204-243.
[27] O. Friedrichs, Weighted essentially non-oscillatory schemes for the interpolation of mean

values on unstructured grids, J. Comput. Phys., 144 (1998), 194-212.
[28] G. Fu and C.-W. Shu, A new troubled-cell indicator for discontinuous Galerkin methods for hyperbolic conservation laws, J. Comput. Phys., 347 (2017), 305-327.
[29] F. Giraldo, J. Hesthaven and T. Warburton, Nodal high-order discontinuous Galerkin methods for spherical shallow water equations, J. Comput. Phys., 181 (2002), 499-525.
[30] W. Guo, R. Nair and J.M. Qiu, A conservative semi-Lagrangian discontinuous Galerkin scheme on the cubed sphere, Mon. Wea. Rev., 142 (2013), 457-475.
[31] D. Hall and R. Nair, Discontinuous Galerkin transport on the spherical Yin-Yang overset mesh, Mon. Wea. Rev., 142 (2013), 264-282.
[32] A. Harten, Multi-resolution analysis for ENO schemes, Institute for Computer Applications in Science and Engineering, NASA Langley Research Center, Hampton, Virginia 23665-5225, Contract No. NAS1-18605, September 1991.
[33] A. Harten, Discrete multi-resolution analysis and generalized wavelets, Appl. Numer. Math., 12 (1993), 153-192.
[34] A. Harten, Adaptive multiresolution schemes for shock computations, Comput. Phys., 115 (1994), 319-338.
[35] A. Harten, Multiresolution algorithms for the numerical solution of hyperbolic conservation laws, Comm. Pure Appl. Math., 48 (1995), 1305-1342.
[36] A. Harten, Multiresolution representation of data: A general framework, SIAM J. Numer. Anal., 33 (1996), 1205-1256.
[37] X.J. He, D.H. Yang and X. Ma, A weighted Runge-Kutta discontinuous Galerkin method for 3D acoustic and elastic wave-field modeling, Commun. Comput. Phys., 28 (2020), 372-400.
[38] J. Hesthaven and T. Warburton, Nodal Discontinuous Galerkin Methods, Springer, New York, 2008.
[39] C. Hu and C.-W. Shu, Weighted essentially non-oscillatory schemes on triangular meshes, J. Comput. Phys., 150 (1999), 97-127.
[40] Z. Jia and S. Zhang, A new high-order discontinuous Galerkin spectral finite element method for Lagrangian gas dynamics in two-dimensions, J. Comput. Phys., 230 (2011), 2496-2522.
[41] G. Jiang and C.-W. Shu, Efficient implementation of weighted ENO schemes, J. Comput. Phys., 126 (1996), 202-228.
[42] L. Krivodonova, J. Xin, J.-F. Remacle, N. Chevaugeon and J.E. Flaherty, Shock detection and limiting with discontinuous Galerkin methods for hyperbolic conservation laws, Appl. Numer. Math., 48 (2004), 323-338.
[43] N. Kroll *et al.* (Editors), ADIGMA-A European Initiative on the Development of Adaptive Higher-Order Variational Methods for Aerospace, Applications Notes on Numerical Fluid Mechanics and Multidisciplinary Design, V113, 2010, Springer.
[44] P.D. Lax, Weak solutions of nonlinear hyperbolic equations and their numerical computation, Commun. Pure Appl. Math., 7 (1954), 159-193.
[45] B. van Leer and S. Nomura, Discontinuous Galerkin for diffusion, in: Proceedings of 17th AIAA Computational Fluid Dynamics Conference, June 6-9, 2005, AIAA-2005-5108.
[46] D. Levy, G. Puppo and G. Russo, Central WENO schemes for hyperbolic systems of conservation laws, M2AN. Math. Model. Numer. Anal., 33 (1999), 547-571.
[47] D. Levy, G. Puppo and G. Russo, Compact central WENO schemes for multidimensional conservation laws, SIAM J. Sci. Comput., 22 (2) (2000), 656-672.
[48] B. Li, Discontinuous Finite Elements in Fluid Dynamics and Heat Transfer, Birkhauser, Basel, 2006.

[49] Z. Li, X. Yu and Z. Jia, The cell-centered discontinuous Galerkin method for Lagrangian compressible Euler equations in two dimensions, Comput. Fluids, 96 (2014), 152-164.
[50] X. Liu, S. Osher and T. Chan, Weighted essentially non-oscillatory schemes, J. Comput. Phys., 115 (1994), 200-212.
[51] J.L. Lou, L. Li, H. Luo and H. Nishikawa, Reconstructed discontinuous Galerkin methods for linear advection-diffusion equations based on first-order hyperbolic system, J. Comput. Phys., 369 (2018), 103-124.
[52] J.L. Lou, X.D. Liu, H. Luo and H. Nishikawa, Reconstructed discontinuous Galerkin methods for hyperbolic diffusion equations on unstructured grids, Commun. Comput. Phys., 25 (2019), 1302-1327.
[53] R. Loubëre, J. Ovadia and R. Abgrall, A Lagrangian discontinuous Galerkin-type method on unstructured meshes to solve hydrodynamics problems, Int. J. Numer. Methods Fluids, 44 (2004), 645-663.
[54] H. Luo, J.D. Baum and R. Lohner, A Hermite WENO-based limiter for discontinuous Galerkin method on unstructured grids, J. Comput. Phys., 225 (2007), 686-713.
[55] R.D. Nair, H.W. Choi and H.M. Tufo, Computational aspects of a scalable high-order discontinuous Galerkin atmospheric dynamical core, Comput. Fluids, 38 (2009), 309-319.
[56] R.D. Nair, M.N. Levy and P.H. Lauritzen, Emerging numerical methods for atmospheric modeling, In P.H. Lauritzen, C. Jablonowski, M.A. Taylor, and R.D. Nair, editors, Numerical Techniques for Global Atmospheric Models, volume 80, pages 189-250. Springer-Verlag, 2011. LNCSE.
[57] R.D. Nair, S. Thomas and R. Loft, A discontinuous Galerkin transport scheme on the cubed sphere, Mon. Wea. Rev., 133 (2005), 814-828.
[58] J. Qiu and C.-W. Shu, Hermite WENO schemes and their application as limiters for Runge-Kutta discontinuous Galerkin method: one dimensional case, J. Comput. Phys., 193 (2003), 115-135.
[59] J. Qiu and C.-W. Shu, Runge-Kutta discontinuous Galerkin method using WENO limiters, SIAM J. Sci. Comput., 26 (2005), 907-929.
[60] J. Qiu and C.-W. Shu, A comparison of troubled-cell indicators for Runge-Kutta discontinuous Galerkin methods using weighted essentially nonoscillatory limiters, SIAM J. Sci. Comput., 27 (2005), 995-1013.
[61] J. Qiu and C.-W. Shu, Hermite WENO schemes and their application as limiters for Runge-Kutta discontinuous Galerkin method II: two dimensional case, Computers & Fluids, 34 (2005), 642-663.
[62] W.H. Reed and T.R. Hill, Triangular mesh methods for neutron transport equation, Tech. Report LA-UR-73-479, Los Alamos Scientific Laboratory, 1973.
[63] C.-W. Shu, Essentially non-oscillatory and weighted essentially non-oscillatory schemes for hyperbolic conservation laws, In Advanced Numerical Approximation of Nonlinear Hyperbolic Equations, B. Cockburn, C. Johnson, C.-W. Shu and E. Tadmor (Editor: A. Quarteroni), Lecture Notes in Mathematics, volume 1697, Springer, 1998, 325-432.
[64] C.-W. Shu, Discontinuous Galerkin methods: general approach and stability, in Numerical Solutions of Partial Differential Equations, S. Bertoluzza, S. Falletta, G. Russo and C.-W. Shu, Advanced Courses in Mathematics CRM Barcelona, Birkhäuser, Basel, 2009, 149-201.
[65] C.-W. Shu, High order weighted essentially non-oscillatory schemes for convection dominated problems, SIAM Review, 51 (2009), 82-126.
[66] C.-W. Shu and S. Osher, Efficient implementation of essentially non-oscillatory shock-capturing schemes, J. Comput. Phys., 77 (1988), 439-471.

[67] G. Sod, A survey of several finite difference methods for systems of nonlinear hyperbolic conservation laws, J. Comput. Phys., 27 (1978), 1-31.
[68] F. Vilar, Cell-centered discontinuous Galerkin discretization for two-dimensional Lagrangian hydrodynamics, Comput. Fluids, 64 (2012), 64-73.
[69] F. Vilar, P.H. Maire and R. Abgrall, Cell-centered discontinuous Galerkin discretizations for two-dimensional scalar conservation laws on unstructured grids and for one-dimensional Lagrangian hydrodynamics, Comput. Fluids, 46 (2010), 498-604.
[70] F. Vilar, P.H. Maire and R. Abgrall, A discontinuous Galerkin discretization for solving the two-dimensional gas dynamics equations written under total Lagrangian formulation on general unstructured grids, J. Comput. Phys., 276 (2014), 188-234.
[71] P. Woodward and P. Colella, The numerical simulation of two-dimensional fluid flow with strong shocks, J. Comput. Phys., 54 (1984), 115-173.
[72] Y.T. Zhang and C.-W. Shu, Third order WENO scheme on three dimensional tetrahedral meshes, Comm. Comput. Phys., 5 (2009), 836-848.
[73] X. Zhong and C.-W. Shu, A simple weighted essentially nonoscillatory limiter for Runge-Kutta discontinuous Galerkin methods, J. Comput. Phys., 232 (2013), 397-415.
[74] J. Zhu and J. Qiu, Hermite WENO schemes and their application as limiters for Runge-Kutta discontinuous Galerkin method III: unstructured meshes, J. Sci. Comput., 39 (2009), 293-321.
[75] J. Zhu and J. Qiu, Runge-Kutta discontinuous Galerkin method using WENO type limiters: three dimensional unstructured meshes, Comm. Comput. Phys., 11 (2012), 985-1005.
[76] J. Zhu, J. Qiu and C.-W. Shu, High-order Runge-Kutta discontinuous Galerkin methods with a new type of multi-resolution WENO limiters, J. Comput. Phys., 404 (2020), 109105.
[77] J. Zhu, J. Qiu, C.-W. Shu and M. Dumbser, Runge-Kutta discontinuous Galerkin method using WENO limiters II: unstructured meshes, J. Comput. Phys., 227 (2008), 4330-4353.
[78] J. Zhu, C.-W. Shu and J. Qiu, High-order Runge-Kutta discontinuous Galerkin methods with a new type of multi-resolution WENO limiters on triangular meshes, Appl. Numer. Math., 153 (2020), 519-539.
[79] J. Zhu and C.-W. Shu, A new type of multi-resolution WENO schemes with increasingly higher order of accuracy, J. Comput. Phys., 375 (2018), 659-683.
[80] J. Zhu and C.-W. Shu, A new type of multi-resolution WENO schemes with increasingly higher order of accuracy on triangular meshes, J. Comput. Phys., 392 (2019), 19-33.
[81] J. Zhu and C.-W. Shu, A new type of third-order finite volume multi-resolution WENO schemes on tetrahedral meshes, J. Comput. Phys., 406 (2020), 109212.
[82] J. Zhu, X. Zhong, C.-W. Shu and J. Qiu, Runge-Kutta discontinuous Galerkin method using a new type of WENO limiters on unstructured meshes, J. Comput. Phys., 248 (2013), 200-220.